Coupling High-Energy Resolution Fluorescence Detected X-ray Absorption Spectroscopy with Microfluidic Cells for in Situ Monitoring of Tungsten Nanoparticles Redox Transformation

Amazigh Ouaksel, Vladimir Vidal, Olivier Proux, Christine Pailles, Jerome Rose, Mélanie F Auffan

Coupling high-energy resolution fluorescence detected X-ray absorption spectroscopy with microfluidic cells for in situ monitoring of tungsten nanoparticles redox transformation

Amazigh Ouaksel [a], *Vladimir Vidal* [a], *Olivier Proux* [b], *Christine Pailles* [a], *Jerome Rose* [a,c], *Melanie Auffan* [a,c,*]

a. CEREGE, CNRS, Aix Marseille Univ, IRD, INRAE, Aix-en-Provence 13545, France

b. OSUG, UAR 832 CNRS - Univ. Grenoble Alpes, IRSTEA, INRAE, Météo-France, Grenoble 38000, France

c. Civil and Environmental Engineering, Duke University, Durham, NC 27708, USA

Keywords

Tungsten, speciation, redox, HERFD XAS, microfluidic, lab-on chip, in situ monitoring

Abstract

Tungsten is a redox-sensitive transition element of strategic importance for many industrial applications. The functionalities of tungsten-based materials are highly dependent on W atomic structure and oxidation state (0, IV and VI), and the same applies to the toxicity of tungsten compounds. However, assessing tungsten speciation and structural changes in complex materials and environmental matrices, poses significant challenges necessitating highly sensitive analysis as well as in situ monitoring at short timescale. We demonstrated that the better energy resolution in HERFD-XAS (energy bandwidth between 1.2 to 1.5 eV) at the L_3-edge with $L_{\alpha 1}$ and $L_{\beta 2}$ emission lines would allow the separation, characterization and quantification of subtle changes in the XAS spectrum associated with specific electronic transitions in W(0), W(IV) and W(VI). Moreover, HERFD-XAS combined with a microfluidic chip proved suitable for in situ monitoring of changes in W redox states with second-scale temporal resolution. We pointed out that such an experimental setup would be particularly useful for providing direct insight into the rapid changes in W speciation that would occur under oxidizing environmental conditions.

37 **Graphical abstract**

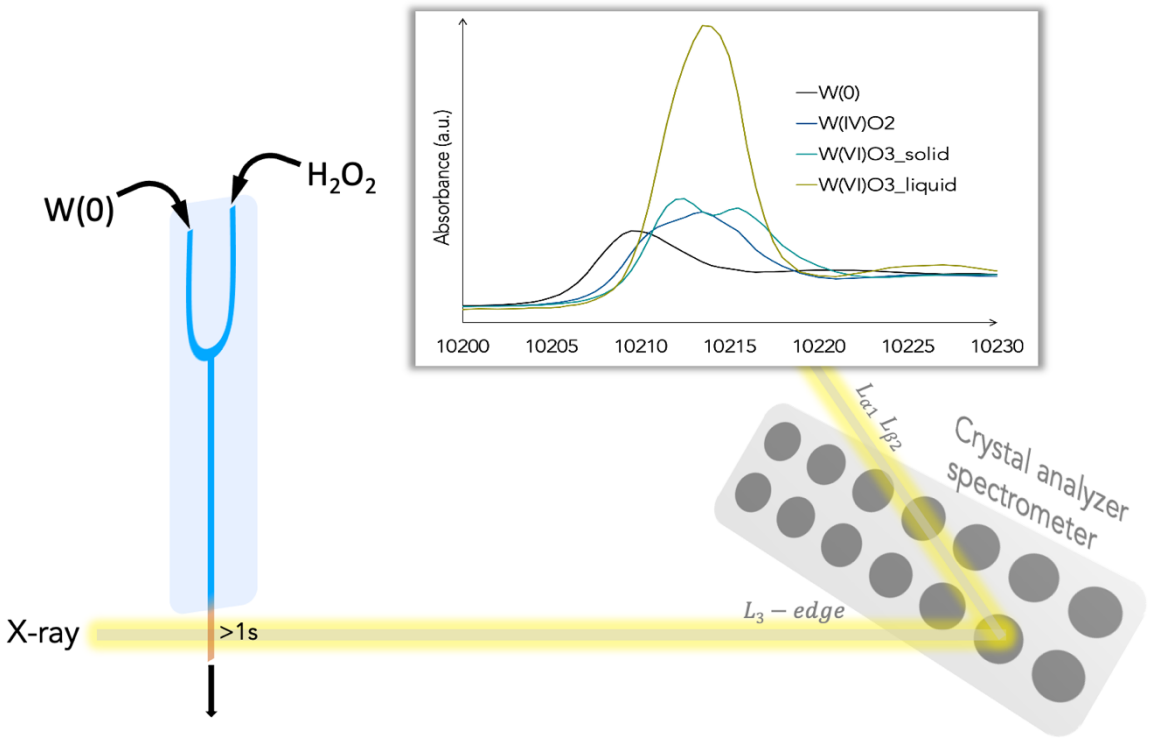

38

39

INTRODUCTION

Tungsten (W), a transition element of Group VIb, has proven to be strategic in a variety of fields ranging from catalysis to electronics, due to the high strength and high melting point, resistance to corrosion and electrochromic properties of W metal, oxides, sulfides and alloys [1]. In particular, tungsten compounds are playing an important role in the energy transition [2] as tungsten-based materials are used for energy storage technologies (as batteries and supercapacitors), energy efficiency in buildings (as devices for smart windows that dynamically control heat and light transmission), renewable energy technologies (as high-efficiency solar cell and wind turbine components), nuclear energy (as structural materials and neutron reflectors), and in energy-efficient lighting applications (halogen lamps with high luminous efficiency and long lifespan, light-emitting diodes,…) [3,4].

Tungsten-based materials functionalities are highly dependent on W atomic structures and oxidation states (W(0), W(IV), W(VI)). But more than the functionalities, the toxicity of tungsten compounds is also speciation-dependent; lower oxidation state compounds being less soluble, less bioavailable, and less toxic compared to those in higher oxidation states as W(VI) [5]. So far, the rate and mechanisms of metallic tungsten oxidative transformations are more documented in acidic or basic media [6–8] compared to biological or environmental media [9–11]. Investigating thoroughly the electronic structure and local environments of tungsten species in materials and environmental samples is then (i) crucial for unraveling the mechanisms behind their functionalities and (ii) essential to assess potential risks and therefore developing appropriate safety guidelines [12,13].

X-ray Absorption Spectroscopy (XAS) has long been a cornerstone technique to probe the oxidation state, coordination environment, ligand identification, and sensitivity to structural changes of metals and metalloids in liquid, solid, and biological matrices. It has been

64 successfully used to identify W speciation in bones [13], biological media [11], materials [14], soils [12]
65 and catalysts [15]. Two commonly used detection modes in XAS at the W edges are conventional
66 total fluorescence yield mode (conv-XAS) [13,16] and High-Energy Resolution Fluorescence
67 Detection mode (HERFD-XAS) [14]. In conv-XAS, detection is typically performed using a
68 solid-state detector (SSD), with energy bandwidth between ~150 to 300 eV, by measuring the
69 main emission lines K_α (including both $K_{\alpha1}$ and $K_{\alpha2}$) or L_α (including both $L_{\alpha1}$ and $L_{\alpha2}$). The
70 detection limit with SSD can reach ~10 to 100 µg.g^{-1} in weight or <1 mmol.L^{-1} [17]. In HERFD-
71 XAS, the detection system is based on a crystal analyzer spectrometer (CAS) that allows a
72 better energy resolution (energy bandwidth typically ranging from 0.2 to 2 eV), reduces
73 background contributions, minimizes fluorescence from higher-energy scattering events, and
74 enhances the sensitivity to weak fluorescence signals compared to conv-XAS [17,18]. HERFD-
75 XAS is performed by measuring the evolution of the intensity of an emission line of interest or
76 part of it ($K_{\alpha1}$, $K_{\beta1,3}$, $L_{\alpha1}$, $L_{\beta2}$...), the CAS being in most cases optimized at the maximum of
77 this emission line. Conv-XAS and HERFD-XAS can be both used for quantitative
78 determination of the oxidation state or coordination number of an element [19]. However, the
79 higher energy resolution and improved signal-to-noise ratio in HERFD-XAS [20] often lead to
80 more accurate quantitative results, particularly when the sample contains multiple species or
81 subtle spectral changes [17].

82 This paper aims to demonstrate the added value of HERFD-XAS compared to conv-XAS when
83 deciphering the different oxidation states of W in mixtures. The higher energy resolution in
84 HERFD-XAS would allow the separation and characterization of subtle changes in the XAS
85 spectrum, such as sharp edges, fine structures, and small shifts associated with specific
86 electronic transitions. As such, the better spectroscopic resolution of HERFD-XAS compared
87 to conv-XAS would allow a more precise quantification of the different oxidation states of W
88 in mixtures. For this, we probed the W L_3-edge by measuring the $L_{\alpha1}$ and $L_{\beta2}$ emission lines

attributed to the electronic transitions from vacant $3d_{5/2}$ ($L_{\alpha 1}$) and 4d ($L_{\beta 2}$) orbitals to $2p_{3/2}$ orbital of the transition metal.

Both conv- and HERFD-XAS can be performed under in situ or operando conditions, allowing time-resolved monitoring of changes in speciation of metals and metalloids under different experimental conditions. Various devices have been developed over the years for real-time analysis. The dispersive XAS technique, which uses a curved crystal to disperse a polychromatic X-ray beam over the sample, enables a detection speed for a complete EXAFS spectrum of 100 ps per spectrum [21]. Quick-XAS, which uses a double-crystal monochromator in continuous mode (instead of step mode), also enables rapid acquisition of a complete spectrum for times of the order of a second [22]. However, whatever the speed at which spectra are acquired, the signal-to-noise ratio of the spectra represents a real limitation, and in all cases, the sample is constantly evolving during acquisition. The integration of microfluidic chips with XAS has emerged as a promising approach, opening up new avenues for studying, in situ and operando, chemical, physico-chemical and biological systems at a microscale [23–25]. Indeed, there has been recently an increasing use of microfluidic cells in environmental applications as water treatment, carbon storage, phosphate immobilization, etc. [26]. These miniaturized experimental devices, commonly referred to as "labs on chips," offer ideal micro-platforms to study complex reaction kinetics, diffusion phenomena, and reaction mechanisms under controlled flow conditions, such as mixing, diffusion, and concentration gradients [26]. Furthermore, one of the main advantages of microfluidic cells in environmental detection and monitoring analysis is their ability to be easily combined with a wide range of optical, electrochemical, and mass spectrometry detection methods [26]. Herein, HERFD-XAS was combined with a microfluid chip for in situ monitoring of changes in W redox states with an enhanced temporal resolution. We suggest that such an experimental set-up would be of interest

in providing direct insight into the fast changes (scale of seconds) in W speciation as it might occur in the oxidizing environmental conditions.

EXPERIMENTAL SECTION

Standard reference compounds and W nanoparticles

Three tungsten reference compounds (W, WO_2, WO_3) were purchased as dry powders from (Merck®). The W powder is 99% certified pure metallic tungsten W(0) with particle sizes smaller than 20 µm and a density ranging from 18.7 to 19.3 $g.cm^{-3}$ at 20 °C. The WO_2 and WO_3 powders are micron-sized with a high purity level (trace metal analysis ≤ 150 ppm) of tungsten (IV) dioxide and tungsten (VI) trioxide respectively.

For microfluidic experiments, we used a suspension of metallic W nanoparticles (nanoW). They were produced via high-energy planetary ball milling following a previously described protocol [11,27,28]. These nanoW are crystallized metallic tungsten with an alpha phase structure. Their size distribution is centered on 216 nm (measured by SEM, see SI, Figure S1) and their surface-specific area measured by Brunauer–Emmett–Teller (BET) method [29] at 3.2 ± 0.16 $m^2.g^{-1}$.

X-ray Absorption Near Edge Structure (XANES)

Conv-XANES spectra at the W L_3-edge (10 207 eV) were obtained on the FAME BM30b beamline, French Absorption spectroscopy beamline in Material and Environmental science at the European Synchrotron Radiation Facility (ESRF) in Grenoble, France (Figure 1 top). A Si(220) two-crystal monochromator was used and energy calibration was carried out by setting the first maximum derivative of the XANES spectrum of a W metal foil at 10 207 eV. The monochromator 1st crystal is liquid-nitrogen cooled, allowing to have an optimal energy selectivity, with a 1st crystal rocking curve close to the Darwin width [30], i.e. 0.52 eV, and so to

obtain spectra with an optimum resolution. For each tungsten reference compounds, 2 to 4 spectra were acquired in fluorescence mode using a 30-element Ge semiconductor detector (Canberra).

HERFD-XANES spectra at the W L_3-edge with $L_{\alpha 1}$ (~8 397 eV) and $L_{\beta 2}$ (~ 9 961 eV) emission lines were obtained on the FAME-UHD BM16 beamline, French Absorption spectroscopy beamline in Material and Environmental sciences at Ultra-High Dilution at the European Synchrotron Radiation Facility (ESRF) in Grenoble, France (Figure 1 bottom). The same monochromator than on BM30b is used (liquid-nitrogen cooled Si(220) first crystal), with the same calibration procedure than for the conv-XANES measurements. For the experiment with the $L_{\alpha 1}$ emission line the beam mode at the ESRF was 7/8+1 (200 mA in top-up mode, with a refill every hour) and the CAS used 14 crystals Si(444). For the experiment performed with the $L_{\beta 2}$ emission line the beam mode at the ESRF was 16 bunch (60-70 mA in top-up mode) and the CAS used 14 crystals Si(555). On both cases, the CAS was aligned with central crystal at 90° with respect to the incident beam, and the other distributed at ±30° with respect to the central one (Figure 1 bottom).

Selected photons, diffracted by each crystal analyzer, were collected by either a 2D hybrid pixel detector (S70 ImXpad) for the alignment procedure and for the reference compounds measurements (thanks to its high dynamic range), or an energy-resolved silicon drift detector (AXAS-M Ketek) for the diluted samples measurements (thanks to its energy resolution which allows to discriminate the diffracted photons of interest from the scattered photons due to other emission lines, Thompson and Compton processes). CAS selected energy bandwidths were estimated by measuring the pseudo-elastic peaks corresponding to each reflection, respectively 1.2 eV and 1.5 eV for $L_{\alpha 1}$ and $L_{\beta 2}$ (Figure 2 top). After CAS calibration, corresponding non-resonant X-ray emission spectroscopy spectra were measured (Figure 2 bottom). In both cases,

positions of the emission lines are found to be independent of the W valence. The emission energy selected by the CAS was then fixed to 8 699.5 eV and 9 964.5 eV for $L_{\alpha 1}$ and $L_{\beta 2}$ HERFD-XAS measurements respectively.

For both conv- and HERFD-XANES analyses, meticulous care was taken during the preparation of the pellets of the solid reference compounds. Indeed, the quality of XANES spectra with minimal signal-to-noise ratio depends on concentration, homogeneity, and thickness of the samples [17,31]. Initially, solid tungsten powders were finely ground and mixed with boron nitride at concentrations of 3000 $mg.kg^{-1}$ for W, WO_2, and WO_3. The diluted powders were homogenized using a homogenizer (WAB-Turbula®, Switzerland) and then pressed into 5 mm diameter-pellets. Radiation damages during spectrum acquisition (photo-oxidation and/or reduction) is a critical concern especially for redox-sensitive elements like tungsten [11] under both conventional and HERFD XAS modes. But as the characteristic features of the HERFD-XANES can be more marked than conv-XANES, the consequences of beam damages on the HERFD-XANES shape may appear enhanced [17]. To minimize these radiation damages, pellets analyses were performed using a cryostat at liquid helium temperature and scans (2 to 4 scans per samples) were measured on different areas of the pellets.

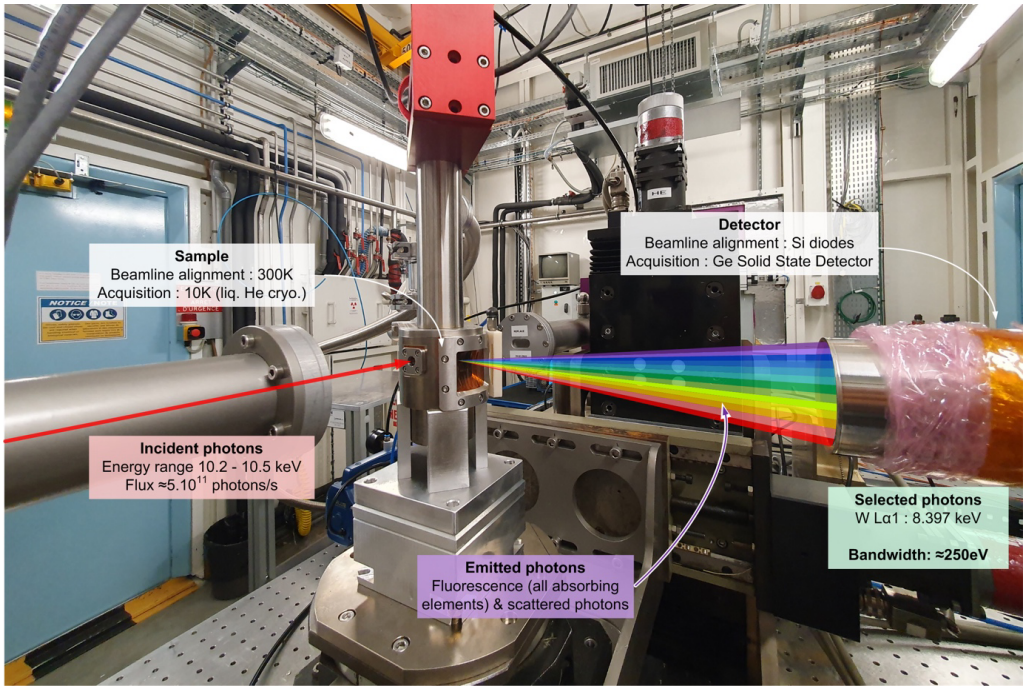

176

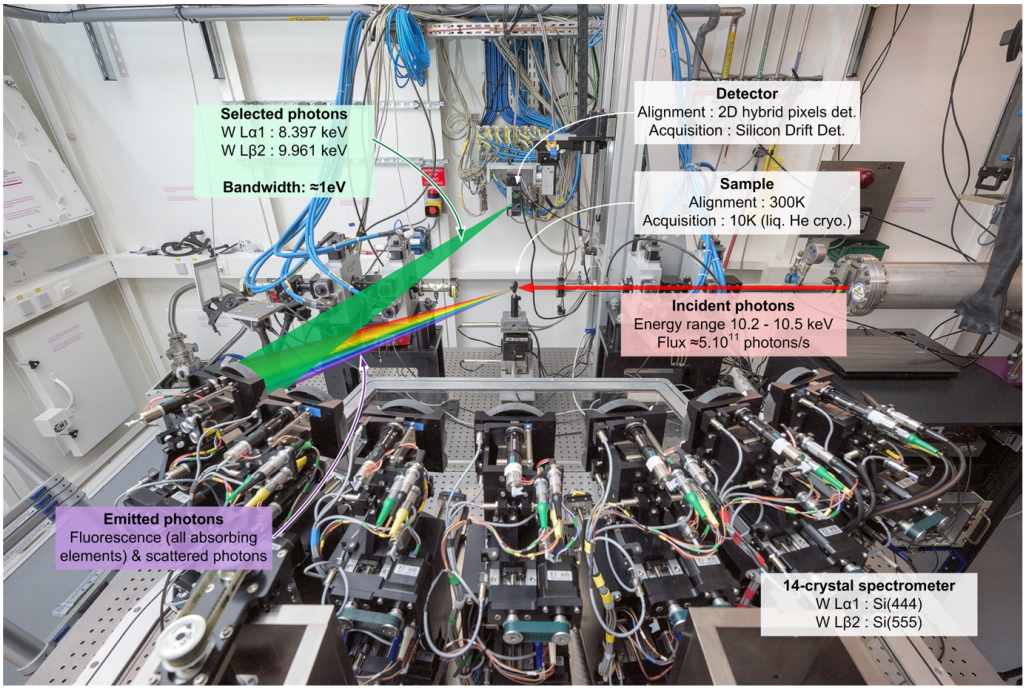

177

178 **Figure 1.** Schemas of the XAS experimental set up of the FAME beamline (BM30b, ESRF)
179 for conventional total fluorescence yield mode (top) and on the FAME-UHD beamline (BM16,
180 ESRF) for HERFD detection mode (bottom).

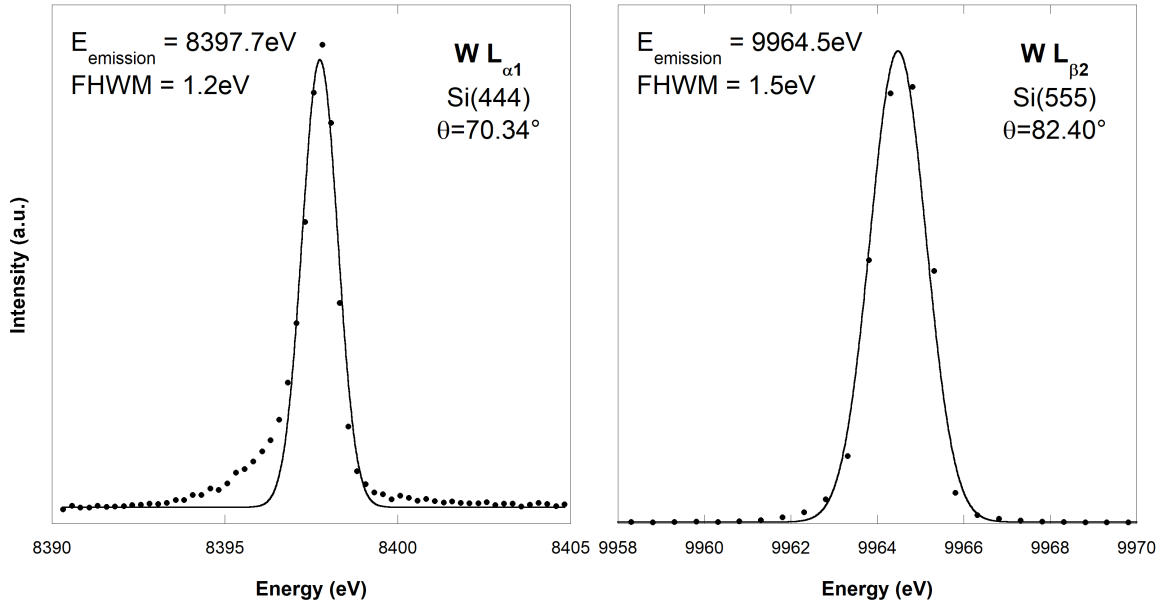

181

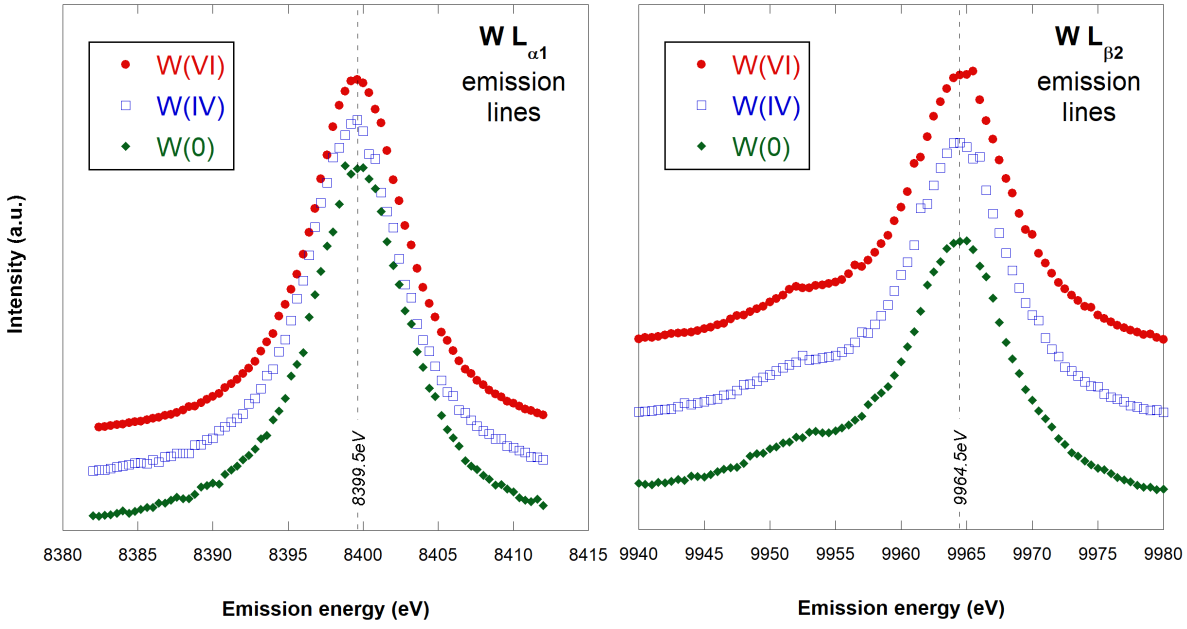

182

183 **Figure 2.** CAS selected energy bandwidths, estimated from the pseudo-elastic peaks and
184 corresponding to the optimization around the $L_{\alpha 1}$ (left) and $L_{\beta 2}$ (right) emission lines (top).
185 Non-resonant X-ray Emission Spectroscopy $L_{\alpha 1}$ (left) and $L_{\beta 2}$ (right) spectra of the three
186 model compounds (bottom). Incident photons energy was fixed to 10 400 eV during XES
187 acquisition.

188

XANES data processing

XANES data reduction was performed with ATHENA software [32]. To assess whether a better spectroscopic resolution by HERFD-XAS would allow a more accurate quantification of the different oxidation states of W in mixtures compared to conv-XAS, we theoretically-generated 3 datasets of more than 30 artificial W multicomponent spectra. These theoretically-generated mixtures were obtained via linear combinations of the conv-XANES or HERFD-XANES ($L_{\alpha 1}$ and $L_{\beta 2}$) spectra of the three W reference compounds described above (W, WO_2 and WO_3). Each theoretically-generated mixture was a combination of the three reference compounds, with a minimum contribution of each compound of 10% of the total mixture. A noise corresponding to 2% of the edge step was added to generate theoretical spectra for further Linear Combination Fit (LCF) analysis. This signal-to-noise ratio was estimated on the edge and post-edge regions of experimental XANES spectra measured on environmental samples (sediments, living organisms) containing 2 to 135 mg $W.kg^{-1}$ (Figure 3). This signal-to-noise is close to the one used in Saurette et al. [33] and 10 times higher than the one used in Proux et al. [17]. LCF was applied to fit the theoretically-generated spectra with the reference compounds (W, WO_2 and WO_3). For LCF, the uncertainty on the amount of each component was estimated to be approximately 10% of the total amount of the target element [34]. Consequently, the attribution of species with values less than 10% should be considered with caution especially if these species do not present striking spectral features.

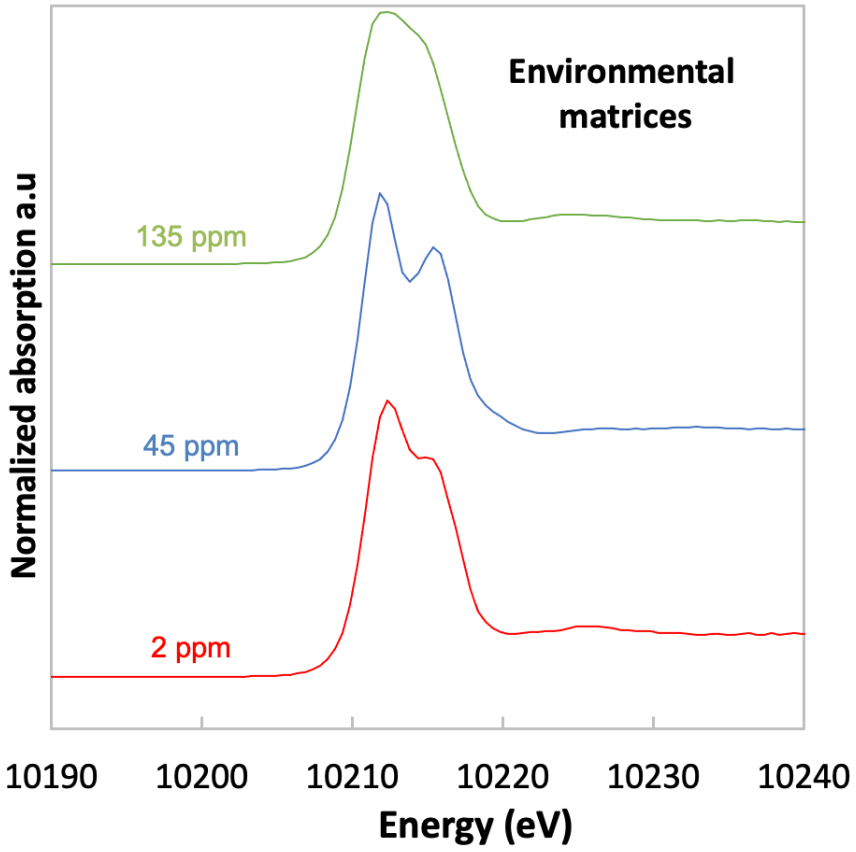

208

209 **Figure 3.** HERFD-XANES (W L3-edge with $L_{\alpha 1}$ emission) spectra of environmental matrices
210 (macrophytes, and sediments initially contaminated with nanoW). The total W concentration
211 in these samples were ranged between 2 to 135 mg W.kg^{-1}.

212 **Microfluidic device design and HERFD-XAS measurements**

213 The microfluidic cell used was manufactured by stereolithography (3D Printer, Formlabs Inc.)
214 using a Clear resin® in order to be X-ray-compatible via an X-ray-transparent window at the
215 cell outlet. The cell contained Y-shaped input channels (800 µm radius tubes) joining into to a
216 115 mm long channel connected to a Kapton tube (10 mm length, 750 µm internal radius).
217 HERFD-XAS measurements were performed in the Kapton window at the L_3-edge with $L_{\beta 2}$
218 emission line with X-ray beam dimensions of 200 µm x 100 µm. The microfluidic unit was set
219 vertically and perpendicularly to the X-ray beam on an x-y-z stage for precise manipulation

and alignment, and in Bragg conditions for the detection by the CAS (see SI, Figure S2). To precisely control fluid flow rates and to probe different reaction times at a second scale the flow was controlled in the two channels by a peristaltic pump (BT100S-1, Lead Fluid).

The first channel of the microfluidic device was connected to a suspension containing the nanoW at a concentration of 1.14 g of $W.L^{-1}$ diluted in Volvic® water with 2 $mmol.L^{-1}$ of potassium hydrogen phthalate ($C_8H_5KO_4$). The pH and Eh of this suspension were 4.6 ± 0.1 and 163 ± 1 mV. The potassium hydrogen phthalate ($C_8H_5KO_4$) was used to prevent the oxidation of the nanoW and to stabilize the pH around 4[35]. To confirm such a chemical stability, this nanoW suspension was circulated in the microfluidic device in closed-loop mode for 3h. In this control experiment, the Eh (142 ± 1 mV) and the pH remained stable (pH between 4.6 ± 0.1 at t_0 and 4.9 ± 0.1 at t_{3h}). No change in the shape or intensity of the HERFD-XANES spectra were observed over time (see SI, Figure S3) confirming the chemical stability of the nanoW during at least 3h.

The second channel of the microfluidic device was connected to a 0.8% H_2O_2 solution. By adjusting the flows in the two channels at 204, 102, 76, 61 $\mu L.s^{-1}$ we monitored the oxidation state of nanoW after 0.75 s, 1.5 s, 2 s, and 2.5 s of interaction with H_2O_2. For the shorter and longer reaction time points of 0.75 s and 2.5 s, the Reynolds numbers in the cell were 213 and 64 respectively, indicating a laminar flow regimen [36]. For each reaction timepoint, 2 to 3 scans (9 min / scan) were averaged to obtain the final HERFD-XANES spectrum. In such configuration, the nanoW exposure to the X-ray beam is 1.2 to 4.2 ms (100 µm of beam height) minimizing beam damage.

Additionally, longer reaction times of 10, 19 and 28 min were examined. In that purpose, the microfluidic device was used in a closed-loop mode: the two input channels and the cell outlet were connected to the same beaker with a constant flow rate of 220 $\mu L.s^{-1}$ in the cell . Forty

mL of the nanoW suspension (at 1.14 g $W.L^{-1}$ diluted in Volvic® water and with 2 $mmol.L^{-1}$ of potassium hydrogen phthalate) were mixed with 0.5 mL of H_2O_2 (30%). pH at 4.4 ± 0.1 and Eh 153 ± 1 mV were measured right after the mixing and reach 3.32 and 213 mV respectively at the end of the 28 min-experiment. In that setup, each HERFD-XANES spectra acquisition last 9 minutes with a one-minute delay prior starting data acquisition. LCF was applied on the first derivatives of the spectra acquired in closed-loop mode. These LCF were performed using the spectra of W(0), WO_2 (IV), and WO_3 (VI) solid reference compounds, and the spectra of dissolved W(VI) obtained after dissolution of WO_3 in milli-Q water followed by an ultrafiltration at 3 KDa (Amicon).

RESULTS and DISCUSSION

Contribution of HERFD-XANES to the detection and quantification of different oxidation states of W in mixtures

The W L_3-edge spectra obtained using the three previously described fluorescence measurements mode and for three W model compounds (W, WO_2, and WO_3) are gathered on Figure 4. The first observation one can make is that, for a given model compound, the spectral resolution of the conventional spectrum is lower than the HERFD ones. Such improvement is well-known and well documented since the first paper by Hämäläinen et al. [37]. Briefly, this was attributed to the relevant core-hole lifetimes involved in the processes. In conventional mode, the final state has a core-hole on the $2p_{3/2}$ level with a lifetime of 4.81 eV [38]. In HERFD mode, the final state has a core-hole on the $3d_{5/2}$ level (case of $L_{\alpha 1}$-HERFD measurement) with a lifetime of 1.7 eV, or on the 4d ones (case of $L_{\beta 2}$-HERFD measurement) with a lifetime of around (4 eV) [38] ; the fluorescence lines corresponding to the $3d_{5/2} \rightarrow 2p_{3/2}$ ($L_{\alpha 1}$) and $4d \rightarrow 2p_{3/2}$ ($L_{\beta 2}$) transitions. HERFD measurements are possible when the energy bandwidth of the fluorescence measurement is lower than these characteristics lifetimes, which is the case here.

In conventional mode, different absorption features are observed at approximately 10 209, 10 213, and 10 214 eV for W(0), W(IV)O_2, and W(VI)O_3 respectively. Despite these shifts in energy, these 3 spectra did not exhibit any marked features. In HERFD mode, a significant shift of the absorption energy was observed between the HERFD-XANES spectra of W(0) (10 207eV) and W(IV)O_2 (10 212 eV) with sharper features compared to conv-XANES. Moreover, the HERFD-XANES spectrum of W(VI)O_3 exhibited a splitting of the white line not detected in conv-XANES, with two distinct peaks at 10 211 and 10 215 eV. Similar sharper features and white line splitting were observed with both $L_{\alpha 1}$ and $L_{\beta 2}$ emission lines. The spectral resolution is slightly better using the $L_{\alpha 1}$ emission line than the $L_{\beta 2}$ one and definitely better when compared with the conventional mode, which is consistent with the fact that the corresponding probed core-hole lifetimes evolve in the same way: 1.7 eV ($L_{\alpha 1}$-HERFD-mode) < 4eV ($L_{\beta 2}$ -HERFD-mode) < 4.81eV (conv-mode).

XANES around the W L_3-edge consists of electron transitions from $2p_{3/2}$ orbitals to vacant 5d orbitals. The two peaks in the white line of W(VI)O_3 are due to the splitting of the 5d states into 5d(t2g) and 5d(eg) sub-bands [16]. In our experimental configuration, the HERFD-XANES spectra were sufficiently resolved to distinguish the splitting of the white line which characterizes the octahedral coordination of W(VI) in WO_3 powders. These findings are consistent with a previous study on the thermochromic phase transition in $CuMo_{1-x}W_xO_4$ solid solutions at the W L_3-edge using resonant X-ray emission spectroscopy [14]. These authors highlighted that the crystal-field splitting energy for octahedral coordination is approximately 3-4 eV. Herein, the obtained value is completely coherent with this splitting.

Such features can also be observed on HERFD-XANES spectra (W L_3-edge with $L_{\alpha 1}$ emission) of environmental samples (macrophytes and sediments containing 2 to 135 mg W.kg^{-1}) initially contaminated with nanoW (Figure 2). In these samples, the white lines are shifted to energies

corresponding to oxidized form of W with more or less marked splitting. In environmental sciences, such a precise discrimination of the local structure around the W atom allowed by HERFD-XAS is crucial since different tungsten oxidation states (0, IV, or VI) and different coordination (tetrahedral or octahedral) can be evidenced.

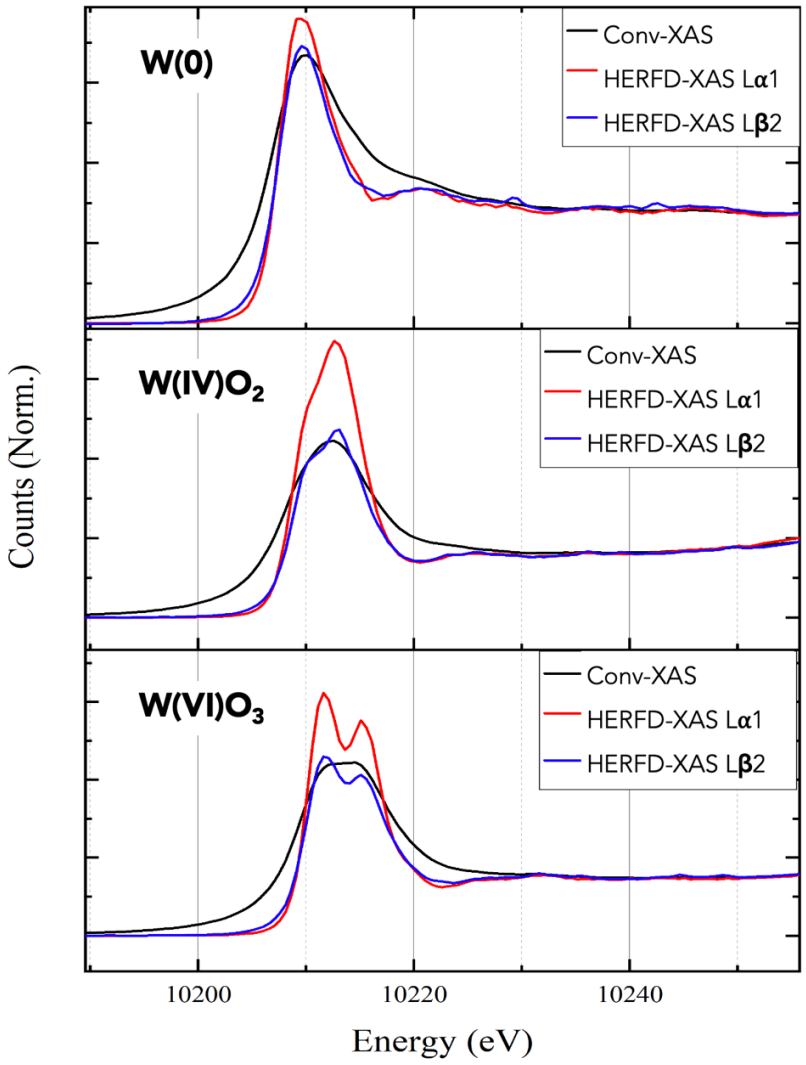

Figure 4. XANES spectra of W(0), W(IV)O_2 and W(VI)O_3 standard reference compounds obtained at the W L_3-edge in both conventional and HERFD modes with $L_{\alpha 1}$ and $L_{\beta 2}$ emission lines respectively.

Quantitative comparison of HERFD and conventional XANES spectroscopy

Following the approaches outlined by Proux et al. and Saurette at al. [17,33] . LCF analysis were carried out on the 3 sets of theoretically-generated spectra acquired in conventional, HERFD $L_{\alpha 1}$ and HERFD $L_{\beta 2}$ modes respectively. Then the standard errors between the theoretical percentage of compounds used and the percentages obtained by LCF were calculated (Figure 5 and Table 1). The standard errors ranged from 1.2 to 2.3 % for the conventional mode while they were ≤ 0.4 % and ≤ 0.9 % for the $L_{\alpha 1}$ and $L_{\beta 2}$ HERFD modes respectively. For W(0) quantification, the standard errors for $L_{\alpha 1}$ and $L_{\beta 2}$ HERFD datasets were 4.5 and 2.5 times lower than conv-mode. For W(IV)O_2 quantification, the standard errors for $L_{\alpha 1}$ and $L_{\beta 2}$ HERFD datasets were 6 and 2.6 times lower than conv-mode. For W(VI)O_3 quantification, the standard errors for $L_{\alpha 1}$ and $L_{\beta 2}$ HERFD datasets were 4 and 1.5 times lower than conv-mode. Such improvements in the precision of LCF were already observed in the literature when using HERFD-XANES spectra at the As and Hg-edges compared to conv-XANES spectra. Proux et al. [17] observed a 8-fold improvement in precision when applying LCF to reconstruct 50 theoretical spectra, using HERFD-XANES spectra of four mercury reference compounds. Saurette et al. [33] calculated the standard error of the LCF with 8 As reference compounds (reconstruction of 3500 computer-generated arsenic mixtures) of the HERFD-XANES and compared to the LCF of the transmission-XANES spectra. The authors observed am improvement in the precision of the LCF when using HERFD-XANES for 4 out of the 8 As reference compounds investigated. These improvements are in good agreement with our study.

The XANES signal of W(IV)O_2 is particularly interesting to consider since it shows the highest improvement in term of quantification using HERFD-XANES. Indeed, spectra reconstruction using LCF is greatly influenced by the spectral features of the reference compounds. Herein, HERFD-XANES spectra of W(IV)O_2 reference compound were sharper and exhibited higher

spectral resolution compared to the conventional mode which resulted in a more precise detection and quantification. This is of major interest, as it enables the W(IV) oxidation state (important intermediary product during the tungsten oxidation and dissolution) to be distinguished from other oxidation states and quantified when studying oxidative transformations of tungsten.

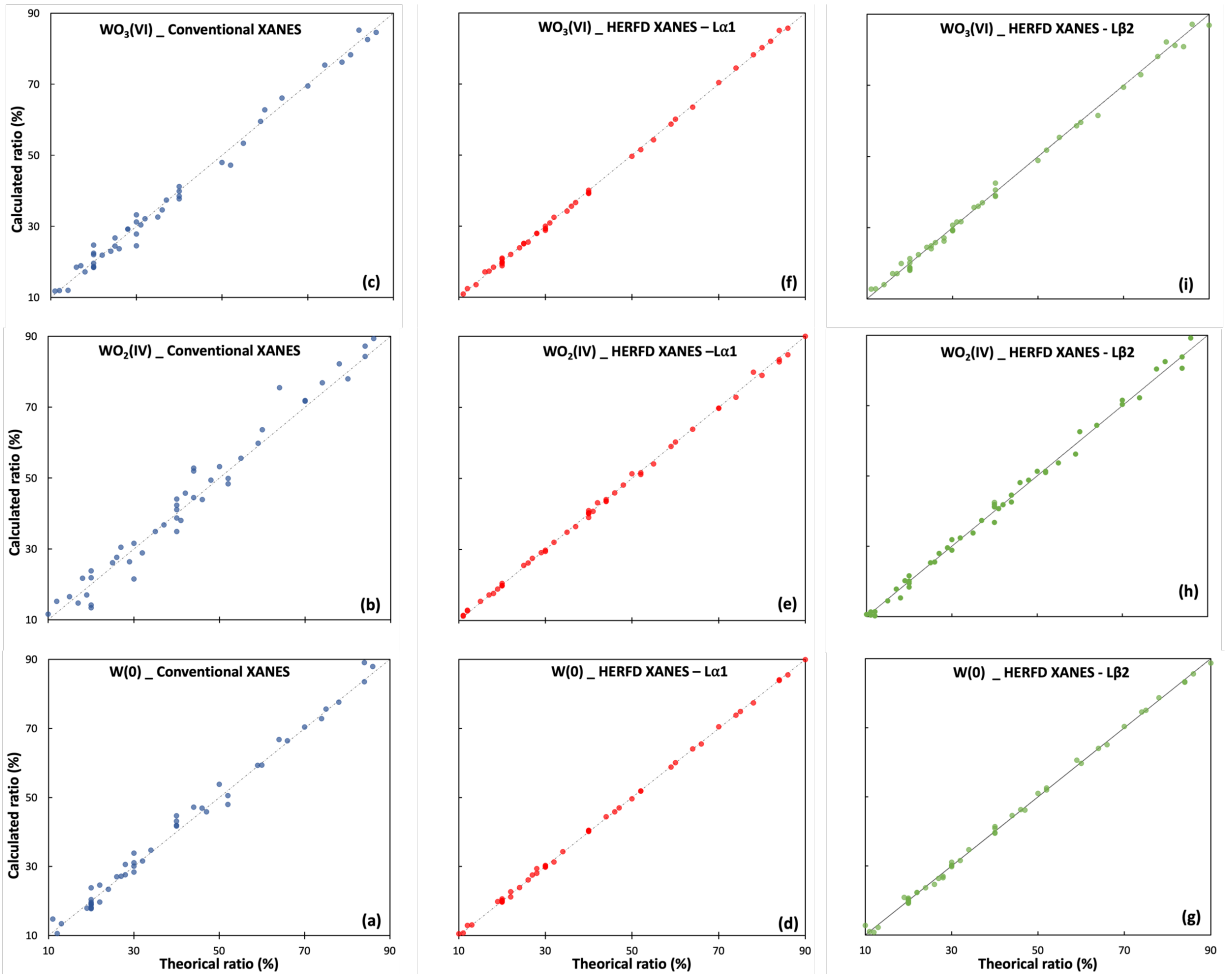

Figure 5. Comparison of the theoretically percentage used to create the theoretically-generated spectra versus the percentages determined from LCF. Results from conv-mode are in blue, from $L_{\alpha 1}$ HERFD-mode in red, and from $L_{\beta 2}$ HERFD-mode are in green. LCF that perfectly replicated the data would result in points that align along a line with a slope of 1 (grey dashed line).

Table 1. Standard errors in percentage for LCF results for each W reference compound, in all theoretically-generated mixtures (conv-XANES and HERFD-XANES). A lower value indicates LCF results close to the theoretical mixture composition.

XANES ACQUISITION MODE	W(0)	$W(IV)O_2$	$W(VI)O_3$
CONVENTIONAL	1.3	2.3	1.2
HERFD $L_{\alpha 1}$	0.3	0.4	0.3
HERFD $L_{\beta 2}$	0.5	0.9	0.8

HERFD-XAS and microfluidic coupling for improved temporal resolution and monitoring of short kinetics transformation of W compounds

In addition to discriminate and quantify the different oxidation stages of W in mixtures, XAS-HERFD can also respond to another challenge in environmental sciences: understanding the tungsten oxidation process on short timescales *in situ*. Indeed, tungsten oxidation kinetics and mechanisms can be complex in the environment, involving multistep reactions and intermediate species formation[11]. These complexities arise from the multiple oxidation states of W, but also from the variations in environmental conditions in term of pH, Eh, temperature, illumination, ionic strength, as well as the presence of other aqueous species or biota. All these parameters may enhance or inhibit W oxidation and consequently its impacts of human and environmental health [39,40].

Recently, Sanles-Sobrido et al.[11] proposed a pathway explaining the oxidation of metallic W particles in biological media with three interfaces defined between the W(0) particle core, a WO_2 subsurface layer, a WO_3 surface layer and W aqueous species [11]. The authors highlighted that even if WO_2 solid phase is not thermodynamically stable in these biological media (pH>6 and positive Eh) [41], it can be considered as an important intermediary product during the

356 tungsten oxidation and dissolution [11,42]. However, Anik and Cansizoglu [43] did not mention WO_2
357 in the dissolution process of WO_3 in more acidic solutions [43]. It is noteworthy that in both
358 Sanles-Sobrido et al. [11] and Anik and Cansizoglu [43] the reaction kinetics are studied at an hour-
359 scale (first time point at 2h and 30 min respectively). Herein, we studied whether the
360 combination of XAS-HERFD at the W L_3-edge with microfluidic chips would provide an
361 interesting platform for time-resolved and *in situ* monitoring of the tungsten oxidation kinetics.

362 The microfluidic cell described above has been set at the end station of the FAME-UHD
363 beamline. The flow was controlled in the two channels to maintain fluid flow rates between
364 204 and 61 $\mu L.s^{-1}$ and to test different reaction times between nanoW (injected in one channel)
365 and H_2O_2 (injected in the second channel) at the second- and minute-scale (Figure 6 left). Of
366 course, these experimental conditions are far from environmentally relevant ones, but they
367 allow us (i) to ensure about the chemical stability of the nanoW at t_0 using the potassium
368 hydrogen phthalate buffer and (ii) to adjust the oxidation kinetics of these nanoW using H_2O_2
369 to a few seconds to test the validity of the proposed approach.

370 We first used the microfluidic cell in a closed-loop setup. The XANES spectra given in figure
371 6 at 10 min, 19 min, and 28 min highlighted respectively the transformation occurring between
372 1-10 minutes, 10-19 min, and 19-28 minutes of interaction between nanoW and H_2O_2. These
373 three spectra were characterized by one large white line shifted to energy corresponding to
374 oxidized species of W. The first derivatives of these experimental HERFD-XANES spectra
375 were fitted using LCF of the spectra of the reference compounds (Figure 6 right). Based on
376 O'Day et al.[44], the uncertainty on the quantification of each contribution is assumed to be about
377 20%. From LCF, metallic W and dissolved W(VI) were detected in the suspension whatever
378 the sampling time at the limit of the uncertainty. The proportion of metallic W decreased from
379 65 % ± 13 (at 10 min) to 39 % ± 8 (at 28 min) and the proportion of dissolved W(VI) increased
380 from 35 % ± 7 (at 10 min) to 61 % ± 12 (at 28 min). Sanles Sobrido et al.[11] proposed an

oxidative dissolution model limited by diffusion from the surface. In such a case, we estimated that the metallic core of the nanoW would be shrunk by ~14 nm between 1 and 10 minutes and by ~29 nm between 19-28 minutes.

Using the open-loop setup, the first reaction timepoint analyzed was at 0.75 s. Between 0.75 to 1.5 s, we did not observe significant change in the oxidation state of nanoW which remained centered on the absorption energy of the W(0) reference compounds. After 2s, an oxidation of the nanoW in contact with H_2O_2 is visible with an enlargement of the white line and shift toward higher absorption energies in line with the signature of $W(IV)O_2$ and $W(VI)O_3$ reference compounds. In particular, the splitting of the white line at 2.5s could highlight the presence of W(VI) with an octahedral geometry [16]. At the end of the XAS acquisition in the open-loop mode, the final pH and Eh were measured at 2.9 ± 0.1 and 261 ± 2 mV respectively. This acidification is related to the protons that are released during the W(0) oxidation in W(VI) in contact with H_2O_2. However, the low signal-to-noise ratio limit deeper discussion and possible quantification using LCF. Indeed, such open-loop setup is relevant to acquire information on changes of nanoW speciation after few seconds of interaction with oxidizing molecules. Although, one drawback to get an acceptable signal-to-noise ratio is that it requires a compromise between the amount of reactant used and the duration of the scans, considering that a minimal fluid flow rate is needed to ensure the particle circulation in the cell.

Allowing the manipulation of the flow rate, of the pH/Eh conditions, and the composition of media (e.g. freshwater, saline water, interstitial water, biological media) in the channels, such HERFD- XAS-microfluidic cell coupling would allow precise and reproducible conditions when investigating the W oxidation kinetics and mechanisms at short (second) timescales. Such coupling is opening new perspectives to decipher the underlying mechanisms governing the rapid oxidation of tungsten in biological and environmental media as well as the durability of the W submicronic materials.

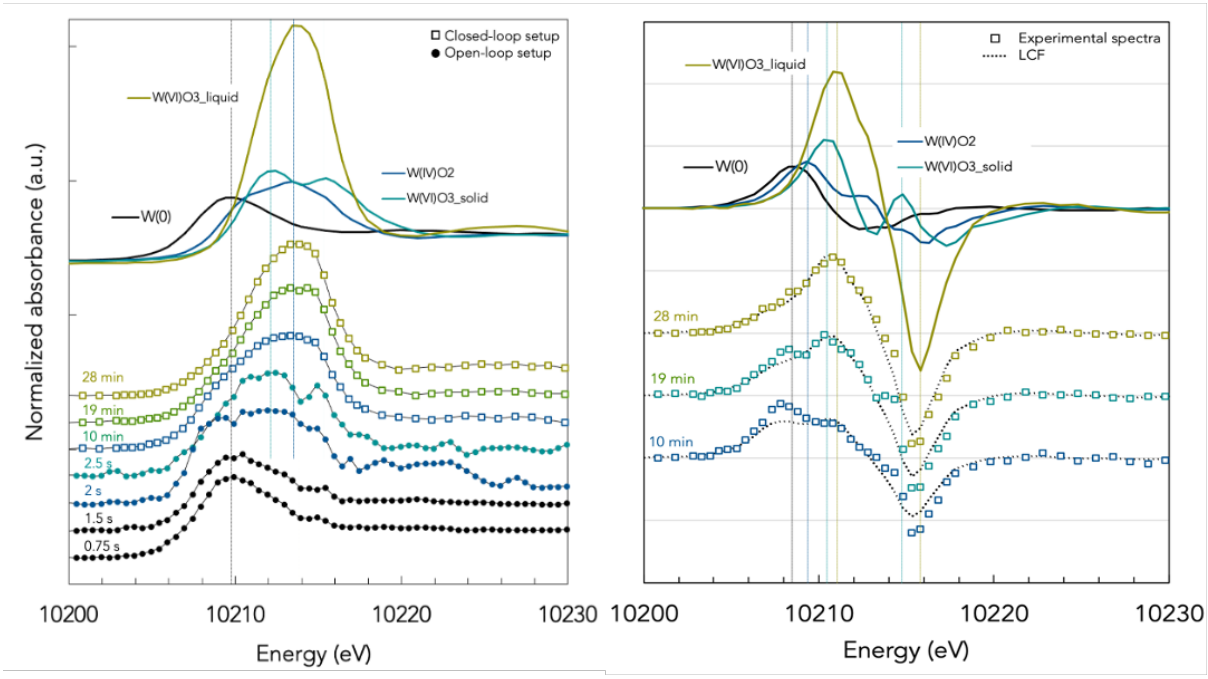

406

407 **Figure 6.** HERFD-XANES spectra (left) and first derivatives (right) at the W L_3-edge with $L_{\beta 2}$

408 emission line measured at increasing reaction times between a nanoW suspension and H_2O_2

409 solution. Reaction times at the second-scale were obtained with the microfluidic cell in open-

410 loop setup (•) while those at the minute-scale were obtained with the closed-loop setup (□).

411 Experimental XANES spectra are compared with W(0), WO_2(IV), and WO_3(VI) solid

412 reference compounds, and with dissolved W(VI) reference obtained after dissolution of WO_3

413 in milli-Q water followed by an ultrafiltration at 3 KDa. First derivatives of the experimental

414 XANES spectra were fitted using linear combination fits (LCF) of the previously cited

415 reference compounds.

416

417

418

419 **CONCLUSION**

420 Tungsten can be exposed to diverse environmental conditions, including freshwater, saline

421 water, soil, sediment as well as biota. Each environment has its unique set of chemical species,

pH levels, redox potentials, and temperature variations, which can significantly influence the oxidation kinetics and mechanisms. Studying tungsten oxidation in such reactive environments requires carefully designed experiments. This papier highlights the ability of coupling microfluidics with HERFD-XAS to fill this gap. We demonstrated that the high energy resolution in HERFD-XAS would allow the separation, characterization, and quantification of subtle changes in the XAS spectrum, such as sharp edges, energy shifts and white line splitting associated with specific electronic transitions of W. We were able to quantify to which extend the better spectroscopic resolution of HERFD-XAS compared to conv-XAS would allow a more accurate estimation of the different oxidation states of W in mixtures. Moreover, HERFD-XAS has been combined with a microfluid chip for in situ monitoring of changes in W redox states with enhanced temporal resolution. We highlighted that such experimental set-up would be particularly valuable to provide direct insight into the fast changes (scale of seconds) in W speciation that would occur in oxidizing conditions.

This study opens new possibilities for monitoring the oxidation–reduction processes at mineral-water interfaces that control the W biogeochemical cycle via electron transfer reactions. In safer by design- or risk assessment-perspectives, understanding the molecular scale process of biogeochemical redox reactions involving W is critical in predicting its fate, mobility, bioavailability, and toxicity in the environment. In the near future, such experimental device could be tuned to tackle the role of organic matter in this process and especially in microbial-mediated transformations. This will be even more important in the context of climate change, during which hotspots for redox reactions are likely to become increasingly active.

ASSOCIATED CONTENT

Supporting Information. X-ray Diffractogram and electron microscopy images of the nanoW, microfluidic cell setup on the FAME-UHD beamline, HERFD-XANES spectra of control nanoW suspension are provided in Supporting Information.

AUTHOR INFORMATION

Corresponding Author

Melanie AUFFAN: auffan@cerege.fr

AUTHOR CONTRIBUTIONS

The manuscript was written through contributions of all authors. All authors have given approval to the final version of the manuscript.

ACKNOWLEDGEMENTS

We thank Mickaël Payet from the CEA for providing the metallic tungsten nanoparticles. This work is a contribution to the OSU-Institut Pythéas. The FAME-UHD project is financially supported by the French "grand emprunt" EquipEx (EcoX, ANR-10-EQPX-27-01), the CEA-CNRS CRG consortium and the INSU CNRS institute. FAME and FAME-UHD are members of the REGEF French Research Infrastructure. Finally, the authors acknowledge the CNRS funding for the IRP iNOVE.

REFERENCES

(1) Wu, C.-M.; Naseem, S.; Chou, M.-H.; Wang, J.-H.; Jian, Y.-Q. Recent Advances in

Tungsten-Oxide-Based Materials and Their Applications. *Front. Mater.* **2019**, *6*, 49. https://doi.org/10.3389/fmats.2019.00049.
(2) Dong, X.; Lu, Y.; Liu, X.; Zhang, L.; Tong, Y. Nanostructured Tungsten Oxide as Photochromic Material for Smart Devices, Energy Conversion, and Environmental Remediation. *Journal of Photochemistry and Photobiology C: Photochemistry Reviews* **2022**, *53*, 100555. https://doi.org/10.1016/j.jphotochemrev.2022.100555.
(3) Deb, S. K. Opportunities and Challenges in Science and Technology of WO3 for Electrochromic and Related Applications. *Solar Energy Materials and Solar Cells* **2008**, *92* (2), 245–258. https://doi.org/10.1016/j.solmat.2007.01.026.
(4) Shinde, P. A.; Jun, S. C. Review on Recent Progress in the Development of Tungsten Oxide Based Electrodes for Electrochemical Energy Storage. *ChemSusChem* **2020**, *13* (1), 11–38. https://doi.org/10.1002/cssc.201902071.
(5) Koutsospyros, A. D.; Koutsospyros, D. A.; Strigul, N.; Braida, W.; Christodoulatos, C. Tungsten: Environmental Pollution and Health Effects. In *Encyclopedia of Environmental Health*; Elsevier, 2019; pp 161–169. https://doi.org/10.1016/B978-0-12-409548-9.11199-6.
(6) Johnson, J. W.; Wu, C. L. The Anodic Dissolution of Tungsten. *J. Electrochem. Soc.* **1971**, *118* (12), 1909. https://doi.org/10.1149/1.2407865.
(7) Lillard, R. S.; Kanner, G. S.; Butt, D. P. The Nature of Oxide Films on Tungsten in Acidic and Alkaline Solutions. *J. Electrochem. Soc.* **1998**, *145* (8), 2718–2725. https://doi.org/10.1149/1.1838704.
(8) Anik, M.; Osseo-Asare, K. Effect of PH on the Anodic Behavior of Tungsten. *J. Electrochem. Soc.* **2002**, *149* (6), B224. https://doi.org/10.1149/1.1471544.
(9) Peuster, M.; Kaese, V.; Wuensch, G.; von Schnakenburg, C.; Niemeyer, M.; Fink, C.; Haferkamp, H.; Hausdorf, G. Composition Andin Vitro Biocompatibility of Corroding Tungsten Coils. *J. Biomed. Mater. Res.* **2003**, *65B* (1), 211–216. https://doi.org/10.1002/jbm.b.10561.
(10) Patrick, E.; Orazem, M. E.; Sanchez, J. C.; Nishida, T. Corrosion of Tungsten Microelectrodes Used in Neural Recording Applications. *Journal of Neuroscience Methods* **2011**, *198* (2), 158–171. https://doi.org/10.1016/j.jneumeth.2011.03.012.
(11) Sanles Sobrido, M.; Bernard, E.; Angeletti, B.; Malard, V.; George, I.; Chaurand, P.; Uboldi, C.; Orsière, T.; Dine, S.; Vrel, D.; Rousseau, B.; Dinescu, G.; Soulas, R.; Herlin, N.; Proux, O.; Grisolia, C.; Rose, J. Oxidative Transformation of Tungsten (W) Nanoparticles Potentially Released in Aqueous and Biological Media in Case of Tokamak (Nuclear Fusion) Lost of Vacuum Accident (LOVA). *Comptes Rendus. Géoscience* **2021**, *352* (8), 539–558. https://doi.org/10.5802/crgeos.41.
(12) Bostick, B. C.; Sun, J.; Landis, J. D.; Clausen, J. L. Tungsten Speciation and Solubility in Munitions-Impacted Soils. *Environ. Sci. Technol.* **2018**, *52* (3), 1045–1053. https://doi.org/10.1021/acs.est.7b05406.
(13) VanderSchee, C. R.; Kuter, D.; Bolt, A. M.; Lo, F.-C.; Feng, R.; Thieme, J.; Chen-Wiegart, Y. K.; Williams, G.; Mann, K. K.; Bohle, D. S. Accumulation of Persistent Tungsten in Bone as in Situ Generated Polytungstate. *Commun Chem* **2018**, *1* (1), 8. https://doi.org/10.1038/s42004-017-0007-6.
(14) Pudza, I.; Kalinko, A.; Cintins, A.; Kuzmin, A. Study of the Thermochromic Phase Transition in CuMo$_{1-X}$W$_x$O$_4$ Solid Solutions at the W L$_3$-Edge by Resonant X-Ray Emission Spectroscopy. *Acta Materialia* **2021**, *205*, 116581. https://doi.org/10.1016/j.actamat.2020.116581.
(15) Howell, J. G.; Li, Y.-P.; Bell, A. T. Propene Metathesis over Supported Tungsten Oxide Catalysts: A Study of Active Site Formation. *ACS Catal.* **2016**, *6* (11), 7728–7738. https://doi.org/10.1021/acscatal.6b01842.
(16) Yamazoe, S.; Hitomi, Y.; Shishido, T.; Tanaka, T. XAFS Study of Tungsten L_1 - and

L $_3$ -Edges: Structural Analysis of WO $_3$ Species Loaded on TiO $_2$ as a Catalyst for Photo-Oxidation of NH $_3$. *J. Phys. Chem. C* **2008**, *112* (17), 6869–6879. https://doi.org/10.1021/jp711250f.
(17) Proux, O.; Irar, M.; Thomas, S.; Aguilar-Tapia, A.; Bazarkina, E. F.; Prat, A.; Auffan, M.; Rose, J.; Hazemann, J.-L. High Energy Resolution Fluorescence Detected X-Ray Absorption Spectroscopy : A New Powerful Structural Tool in Environmental Biogeochemistry Sciences Supplementary Information. **2017**.
(18) Hazemann, J.-L.; Proux, O.; Nassif, V.; Palancher, H.; Lahera, E.; Da Silva, C.; Braillard, A.; Testemale, D.; Diot, M.-A.; Alliot, I.; Del Net, W.; Manceau, A.; Gélébart, F.; Morand, M.; Dermigny, Q.; Shukla, A. High-Resolution Spectroscopy on an X-Ray Absorption Beamline. *J Synchrotron Rad* **2009**, *16* (2), 283–292. https://doi.org/10.1107/S0909049508043768.
(19) Swarbrick, J. C.; Skyllberg, U.; Karlsson, T.; Glatzel, P. High Energy Resolution X-Ray Absorption Spectroscopy of Environmentally Relevant Lead(II) Compounds. *Inorg. Chem.* **2009**, *48* (22), 10748–10756. https://doi.org/10.1021/ic9015299.
(20) Abe, H.; Aquilanti, G.; Boada, R.; Bunker, B.; Glatzel, P.; Nachtegaal, M.; Pascarelli, S. Improving the Quality of XAFS Data. *J Synchrotron Rad* **2018**, *25* (4), 972–980. https://doi.org/10.1107/S1600577518006021.
(21) Pascarelli, S.; Mathon, O.; Muñoz, M.; Mairs, T.; Susini, J. Energy-Dispersive Absorption Spectroscopy for Hard-X-Ray Micro-XAS Applications. *J Synchrotron Rad* **2006**, *13* (5), 351–358. https://doi.org/10.1107/S0909049506026938.
(22) Mathon, O.; Beteva, A.; Borrel, J.; Bugnazet, D.; Gatla, S.; Hino, R.; Kantor, I.; Mairs, T.; Munoz, M.; Pasternak, S.; Perrin, F.; Pascarelli, S. The Time-Resolved and Extreme Conditions XAS (TEXAS) Facility at the European Synchrotron Radiation Facility: The General-Purpose EXAFS Bending-Magnet Beamline BM23. *J Synchrotron Rad* **2015**, *22* (6), 1548–1554. https://doi.org/10.1107/S1600577515017786.
(23) Avaro, J.; Moon, E. M.; Rose, J.; Rose, A. L. Calcium Coordination Environment in Precursor Species to Calcium Carbonate Mineral Formation. *Geochimica et Cosmochimica Acta* **2019**, *259*, 344–357. https://doi.org/10.1016/j.gca.2019.05.041.
(24) Probst, J.; Borca, C. N.; Newton, M. A.; van Bokhoven, J.; Huthwelker, T.; Stavrakis, S.; deMello, A. In Situ X-Ray Absorption Spectroscopy and Droplet-Based Microfluidics: An Analysis of Calcium Carbonate Precipitation. *ACS Meas. Sci. Au* **2021**, *1* (1), 27–34. https://doi.org/10.1021/acsmeasuresciau.1c00005.
(25) Wielinski, J.; Jimenez-Martinez, J.; Göttlicher, J.; Steininger, R.; Mangold, S.; Hug, S. J.; Berg, M.; Voegelin, A. Spatiotemporal Mineral Phase Evolution and Arsenic Retention in Microfluidic Models of Zerovalent Iron-Based Water Treatment. *Environ. Sci. Technol.* **2022**, *56* (19), 13696–13708. https://doi.org/10.1021/acs.est.2c02189.
(26) Yew, M.; Ren, Y.; Koh, K. S.; Sun, C.; Snape, C. A Review of State-of-the-Art Microfluidic Technologies for Environmental Applications: Detection and Remediation. *Global Challenges* **2019**, *3* (1), 1800060. https://doi.org/10.1002/gch2.201800060.
(27) El-Kharbachi, A.; Chêne, J.; Garcia-Argote, S.; Marchetti, L.; Martin, F.; Miserque, F.; Vrel, D.; Redolfi, M.; Malard, V.; Grisolia, C.; Rousseau, B. Tritium Absorption/Desorption in ITER-like Tungsten Particles. *International Journal of Hydrogen Energy* **2014**, *39* (20), 10525–10536. https://doi.org/10.1016/j.ijhydene.2014.05.023.
(28) Dine, S.; Aïd, S.; Ouaras, K.; Malard, V.; Odorico, M.; Herlin-Boime, N.; Habert, A.; Gerbil-Margueron, A.; Grisolia, C.; Chêne, J.; Pieters, G.; Rousseau, B.; Vrel, D. Synthesis of Tungsten Nanopowders: Comparison of Milling, SHS, MASHS and Milling-Induced Chemical Processes. *Advanced Powder Technology* **2015**, *26* (5), 1300–1305. https://doi.org/10.1016/j.apt.2015.07.004.
(29) Dollimore, D.; Spooner, P.; Turner, A. The Bet Method of Analysis of Gas

Adsorption Data and Its Relevance to the Calculation of Surface Areas. *Surface Technology* **1976**, *4* (2), 121–160. https://doi.org/10.1016/0376-4583(76)90024-8.
(30) Proux, O.; Nassif, V.; Prat, A.; Ulrich, O.; Lahera, E.; Biquard, X.; Menthonnex, J.-J.; Hazemann, J.-L. Feedback System of a Liquid-Nitrogen-Cooled Double-Crystal Monochromator: Design and Performances. *J Synchrotron Rad* **2006**, *13* (1), 59–68. https://doi.org/10.1107/S0909049505037441.
(31) Nehzati, S.; Dolgova, N. V.; James, A. K.; Cotelesage, J. J. H.; Sokaras, D.; Kroll, T.; George, G. N.; Pickering, I. J. High Energy Resolution Fluorescence Detected X-Ray Absorption Spectroscopy: An Analytical Method for Selenium Speciation. *Anal. Chem.* **2021**, *93* (26), 9235–9243. https://doi.org/10.1021/acs.analchem.1c01503.
(32) Ravel, B.; Newville, M. *ATHENA* , *ARTEMIS* , *HEPHAESTUS* : Data Analysis for X-Ray Absorption Spectroscopy Using *IFEFFIT*. *J Synchrotron Rad* **2005**, *12* (4), 537–541. https://doi.org/10.1107/S0909049505012719.
(33) Saurette, E. M.; Frinfrock, Y. Z.; Verbuyst, B.; Blowes, D. W.; McBeth, J. M.; Ptacek, C. J. Improved Precision in As Speciation Analysis with HERFD-XANES at the As *K* -Edge: The Case of As Speciation in Mine Waste. *J Synchrotron Rad* **2022**, *29* (5), 1198–1208. https://doi.org/10.1107/S1600577522007068.
(34) Kirpichtchikova, T. A.; Manceau, A.; Spadini, L.; Panfili, F.; Marcus, M. A.; Jacquet, T. Speciation and Solubility of Heavy Metals in Contaminated Soil Using X-Ray Microfluorescence, EXAFS Spectroscopy, Chemical Extraction, and Thermodynamic Modeling. *Geochimica et Cosmochimica Acta* **2006**, *70* (9), 2163–2190. https://doi.org/10.1016/j.gca.2006.02.006.
(35) *Test No. 111: Hydrolysis as a Function of PH*; OECD Publishing, 2004.
(36) Marle, L.; Greenway, G. M. Microfluidic Devices for Environmental Monitoring. *TrAC Trends in Analytical Chemistry* **2005**, *24* (9), 795–802. https://doi.org/10.1016/j.trac.2005.08.003.
(37) Hämäläinen, K.; Siddons, D. P.; Hastings, J. B.; Berman, L. E. Elimination of the Inner-Shell Lifetime Broadening in x-Ray-Absorption Spectroscopy. *Phys. Rev. Lett.* **1991**, *67* (20), 2850–2853. https://doi.org/10.1103/PhysRevLett.67.2850.
(38) Campbell, J. L.; Papp, T. WIDTHS OF THE ATOMIC K–N7 LEVELS. *Atomic Data and Nuclear Data Tables* **2001**, *77* (1), 1–56. https://doi.org/10.1006/adnd.2000.0848.
(39) George, I.; Uboldi, C.; Bernard, E.; Sobrido, M.; Dine, S.; Hagège, A.; Vrel, D.; Herlin, N.; Rose, J.; Orsière, T.; Grisolia, C.; Rousseau, B.; Malard, V. Toxicological Assessment of ITER-Like Tungsten Nanoparticles Using an In Vitro 3D Human Airway Epithelium Model. *Nanomaterials* **2019**, *9* (10), 1374. https://doi.org/10.3390/nano9101374.
(40) Uboldi, C.; Sanles Sobrido, M.; Bernard, E.; Tassistro, V.; Herlin-Boime, N.; Vrel, D.; Garcia-Argote, S.; Roche, S.; Magdinier, F.; Dinescu, G.; Malard, V.; Lebaron-Jacobs, L.; Rose, J.; Rousseau, B.; Delaporte, P.; Grisolia, C.; Orsière, T. In Vitro Analysis of the Effects of ITER-Like Tungsten Nanoparticles: Cytotoxicity and Epigenotoxicity in BEAS-2B Cells. *Nanomaterials* **2019**, *9* (9), 1233. https://doi.org/10.3390/nano9091233.
(41) Nave, M. I.; Kornev, K. G. Complexity of Products of Tungsten Corrosion: Comparison of the 3D Pourbaix Diagrams with the Experimental Data. *Metall Mater Trans A* **2017**, *48* (3), 1414–1424. https://doi.org/10.1007/s11661-016-3888-6.
(42) Kelsey, G. S. The Anodic Oxidation of Tungsten in Aqueous Base. *J. Electrochem. Soc.* **1977**, *124* (6), 814–819. https://doi.org/10.1149/1.2133418.
(43) Anik, M.; Cansizoglu, T. Dissolution Kinetics of WO3 in Acidic Solutions. *J Appl Electrochem* **2006**, *36* (5), 603–608. https://doi.org/10.1007/s10800-006-9113-3.
(44) O'Day, P. A.; Rivera, N.; Root, R.; Carroll, S. A. X-Ray Absorption Spectroscopic Study of Fe Reference Compounds for the Analysis of Natural Sediments. *American Mineralogist* **2004**, *89* (4), 572–585. https://doi.org/10.2138/am-2004-0412.

617